Received: Added at production | Revised: Added at production | Accepted: Added at production

DOI: xxx/xxxx

ARTICLE TYPE

Performance assessment of the augmented finite element method for the modelling of weak discontinuities

Simon Essongue*[1] | Guillaume Couégnat[2] | Eric Martin[2]

[1]Institut Clément Ader (ICA), Université de Toulouse, CNRS-INSA-ISAE-Mines Albi-UPS, Toulouse, France
[2]Laboratoire des Composites Thermostructuraux, UMR5801 CNRS /Univ. Bordeaux/Safran/CEA, Bordeaux, France

Correspondence
*Simon Essongue Email: simon.essongue-boussougou@isae-supaero.fr

Present Address
3 Rue Caroline Aigle, 31400 Toulouse, France

Summary

This paper investigates the convergence properties of the augmented finite element method (AFEM). The AFEM is here used to model weak discontinuities independently of the underlying mesh. One noticeable advantage of the AFEM over other partition of unity methods is that it does not introduce additional global unknowns. Numerical 2D experiments illustrate the performance of the method and draw comparisons with the finite element method (FEM) and the non-conforming FEM. It is shown that the AFEM converges with an error of $\mathcal{O}(h^{0.5})$ in the energy norm. The non-conforming FEM shares the same property while the FEM converges at $\mathcal{O}(h)$. Yet, the AFEM is on par with the FEM for certain homogenization problems.

KEYWORDS:
embedded discontinuities, embedded finite elements, weak discontinuities, augmented finite element method

1 | INTRODUCTION

Weak discontinuities are surfaces across which the strain field has a jump while the displacement field remains continuous. These discontinuities may result from strain localization phenomena such as shear bands in metals or kink bands in fibre reinforced composite materials [1,2]. Necessary conditions for their appearance are not discussed here and we refer the interested reader to [3,4,5] and references therein. In addition, any interface located in between materials with different mechanical properties is also a weak discontinuity surface. This work deals with this latter situation where the location of weak discontinuities is known beforehand.

Modelling of heterogeneous materials with complex microstructure, such as composites, requires to represent an arbitrary number of material interfaces. The standard finite element method (FEM) imposes the use of conforming meshes that explicitly describe these interfaces, which may cause the discretization process to be time-consuming or burdensome.

To overcome this meshing difficulty, variants of the standard FEM allowing to embed weak discontinuities within elements have thus been developed. They are labelled as "enriched finite element methods" [6,7,8]. The presence of discontinuities is modelled by introducing additional degrees of freedom (DOF). Two main families can be distinguished depending on the support of the enrichment: either the nodes or the elements [9,10]. Some of the most popular nodal enrichment methods include the extended finite element method (XFEM) [11,12], the generalized finite element method (GFEM) [13,14] and the phantom node method (PNM) [15,16,17]. These approaches are special instances of the partition of unity method (PUM) [18,19] and are now recognised to be closely related [20,17,7,21,22]. In this work, the term XFEM will refer to the aforementioned methods. They were shown to yield optimal convergence rates with mesh refinement and to be as accurate as the FEM when dealing with weak discontinuities [23].

The development of element-level enrichment methods started in the early 90's [24,25]. Due to the nature of the enrichment, the additional DOF can be condensed at the element level. Hence, the enriched problem is not larger than the original one, no matter the number of discontinuities, which is an advantage when compared with the XFEM. The resulting approaches are

called embedded finite element methods or finite elements with embedded discontinuities (EFEM)[26,27,28,8,29]. Yet, in contrast to the FEM or the XFEM, EFEMs are non-conforming methods: they induce a violation of the interelement continuity of the displacement field.

A slight modification of the standard FEM also enables to somewhat model material interfaces without meshing them. Their effect is taken into account by assigning different material properties to the integration points of the elements according to their position with respect to the discontinuity. Yet, this strategy is known to lead to suboptimal convergence rates since the approximation space does not contain any weak discontinuity[30]. This approach appears under various names in the literature such as "non-conforming FEM"[23], "voxel-based FEM"[31] or "macro finite element"[32]. The finite cell method (FCM)[33,34] also makes use of this strategy to model weak discontinuities. The term "non-conforming FEM" will be used to designate these methods in the remainder of this work.

EFEMs are predominantly employed to model strong discontinuities[26]. Successful applications dealing with weak discontinuities can be found in the literature[35,36,37,38] but no information on the convergence rates of the methods are reported. Moreover, the particular formulation of the EFEMs used in the aforementioned references differ. If these approaches have proven to be valuable tools with a broad scope of application, key information is still missing to widen their acceptance and use, and it remains unclear how to decide which EFEM is best suited to solve a given problem, or how it compares with other variants. This knowledge gap reflects the primary use of EFEMs: they are principally applied to nonlinear problems involving propagation of cohesive cracks or plasticity induced shear bands. Closed-form solutions to these problems are often out of reach and the development of error estimators in these cases is fairly complex[39]. Ensuring that a numerical method is convergent as well as deriving its convergence properties is nevertheless of prime interest. Therefore, the aim of this study is to provide a precise insight into the performances of the EFEM to model perfectly bonded interfaces. Comparisons with the standard FEM and the non-conforming FEM will also be drawn. These numerical methods have been implemented in an in-house FE code to allow for a fair comparison.

Our study will be focused on the particular EFEM formulation proposed by Yang and co-workers, the augmented finite element method (AFEM)[40,36]. It is free from stress-locking and, contrary to numerous EFEMs, it does not require to assume any enhanced strain modes[28,29,41]. It further departs from other EFEMs on several aspects: it allows to model weak and strong discontinuities, as well as the transition from the former to the latter, and permits to embed multiple discontinuities within an element. The relative simplicity of the AFEM allowed the authors to extend it to thermomechanical applications[42], dynamic loadings[43,44] as well as three-dimensional studies of heterogeneous materials[45,46]. The method has been implemented as a user element in Abaqus and appeared to be approximately 50 times faster than the phantom node method natively implemented in this software[47].

An outline of the paper is as follows. In Section 2, the use of the FEM and the non-conforming FEM made in this study are detailed. In Section 3, the general AFEM framework for the modelling of weak discontinuities is recalled. Section 3.1 presents the strong and weak forms of the problem as well as the condensed discretized equilibrium equations. Section 3.2 specifies which augmented finite elements are employed in the present study. The accuracy and the convergence rate of the AFEM are investigated through numerical experiments in Section 4 and 5. The condition number of AFEM stiffness matrices is investigated in Section 6. The benefits and the limits of the AFEM are finally discussed in Section 7.

2 | MODELLING OF WEAK DISCONTINUITIES WITH THE STANDARD FEM

Typical ways of handling weak discontinuity surfaces with the finite element method are schematised in Figure 1 and detailed next. The discretized equilibrium equations of the standard FEM are not recalled here and we refer the interested reader to reference textbooks[48].

2.1 | Discretizations matching the material interfaces: the standard FEM

The most straightforward and accurate manner to represent weak discontinuity surfaces with finite elements is to mesh them explicitly, see Figure 1 T3 and Q4. Indeed, optimal convergence rate of the solution with mesh refinement is ensured if weak discontinuities are located on the finite elements boundaries. Automatic meshing of complex (micro)structures relies on tailored algorithms[49,50] and GMSH[51] has been employed to generate the meshes used in this study. The FE meshes are either composed

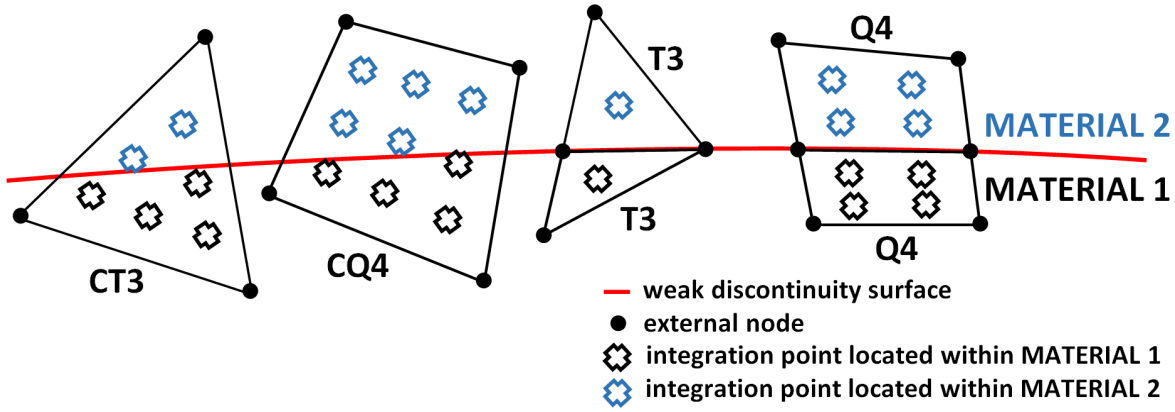

FIGURE 1 Finite elements used in this study to represent a weak discontinuity, from left to right: triangular cell (CT3), quadrilateral cell (CQ4), triangular finite element (T3), quadrilateral finite element (Q4)

of linear triangular elements with one integration point (T3) or bilinear quadrilateral elements with a 2×2 Gauss integration scheme (Q4), see Figure 1 T3 and Q4.

2.2 | Discretizations not matching the weak discontinuity surfaces: the non-conforming FEM

The automatic meshing of complex microstructures may fail or generate highly distorted meshes. Some authors thus do not to mesh the weak discontinuities and let them "cross" the standard finite elements. The effect of the underlying discontinuity is then taken into account by assigning different material properties to the integration points of the crossed elements, according to their position with respect to the weak discontinuity, see Figure 1 CT3 and CQ4. As stated in the introduction this approach will be termed the "non-conforming FEM" in the remainder of this work. The finite elements crossed by a weak discontinuity will be called "cells" in what follows. A T3 and a Q4 crossed by a discontinuity are named CT3 and CQ4 respectively. The CT3 is integrated with a 6-point integration scheme while the CQ4 uses a 3×3 Gauss scheme, see Figure 1 CT3 and CQ4. Although they may use the same meshes, notable differences do exist between the non-conforming FEM and the AFEM. Conversely to the latter, the former does not model any weak discontinuity but it induces no interlement discontinuities.

3 | MODELLING OF WEAK DISCONTINUITIES WITH THE AFEM

3.1 | Strong form, weak form and condensed discretized equilibrium equation

The reference situation to be considered is schematised in Figure 2. Let Ω be the domain occupied by a solid. A material point inside the domain is labelled as $\mathbf{x} \in \Omega$. A weak discontinuity surface Γ_c splits Ω into two subdomains Ω^+ and Ω^-. The prescribed external tractions $\mathbf{t}^+_{\text{ext}}$ and $\mathbf{t}^-_{\text{ext}}$ are applied on boundary $\Gamma_t = \Gamma^+_t \cup \Gamma^-_t$ whereas the displacements $\bar{\mathbf{u}}^+$ and $\bar{\mathbf{u}}^-$ are imposed on boundary $\Gamma_u = \Gamma^+_u \cup \Gamma^-_u$. The domains on both sides of the discontinuity are assumed to be elastic and homogeneous, yet Ω^+ and Ω^- can be made of different materials. We further assume small strain and displacement conditions. In the absence of body forces the field equations governing the boundary value problem obey the following relations

$$\boldsymbol{\nabla}\boldsymbol{\sigma}^+(\mathbf{x}) = \mathbf{0} \qquad \mathbf{x} \in \Omega^+ \qquad \boldsymbol{\nabla}\boldsymbol{\sigma}^-(\mathbf{x}) = \mathbf{0} \qquad \mathbf{x} \in \Omega^- \tag{1}$$

$$\boldsymbol{\sigma}^+(\mathbf{x}).\mathbf{n}^+(\mathbf{x}) = \mathbf{t}^+_{\text{ext}}(\mathbf{x}) \qquad \mathbf{x} \in \Gamma^+_t \qquad \boldsymbol{\sigma}^-(\mathbf{x}).\mathbf{n}^-(\mathbf{x}) = \mathbf{t}^-_{\text{ext}}(\mathbf{x}) \qquad \mathbf{x} \in \Gamma^-_t \tag{2}$$

$$\mathbf{u}^+(\mathbf{x}) = \bar{\mathbf{u}}^+(\mathbf{x}) \qquad \mathbf{x} \in \Gamma^+_u \qquad \mathbf{u}^-(\mathbf{x}) = \bar{\mathbf{u}}^-(\mathbf{x}) \qquad \mathbf{x} \in \Gamma^-_u \tag{3}$$

$$\mathbf{t}^+_{\text{int}}(\mathbf{x}) = \boldsymbol{\sigma}^+(\mathbf{x}).\mathbf{n}^+(\mathbf{x}) \qquad \mathbf{x} \in \Gamma_c \qquad \mathbf{t}^-_{\text{int}}(\mathbf{x}) = \boldsymbol{\sigma}^-(\mathbf{x}).\mathbf{n}^-(\mathbf{x}) \qquad \mathbf{x} \in \Gamma_c \tag{4}$$

$\boldsymbol{\sigma}^+$ and $\boldsymbol{\sigma}^-$ stand for the stress fields in Ω^+ and Ω^- respectively, $\mathbf{t}^+_{\text{int}}$ and $\mathbf{t}^-_{\text{ext}}$ are the tractions along the discontinuity surface Γ_c whereas $\mathbf{n}^+$ and $\mathbf{n}^-$ are the outward pointing normals of Ω^+ and Ω^- respectively. The constitutive law and the strain-displacement

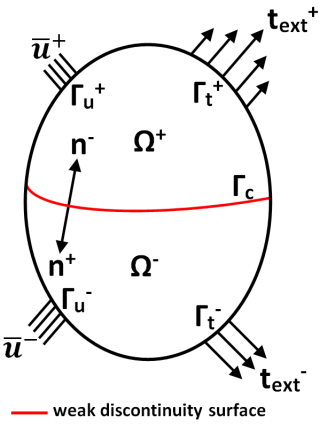

FIGURE 2 Solid body crossed by a weak discontinuity surface

equations for the two subdomains read

$$\boldsymbol{\sigma}^+(\mathbf{x}) = \mathbf{C}^+ : \boldsymbol{\epsilon}^+(\mathbf{x}) \qquad \mathbf{x} \in \Omega^+ \qquad \boldsymbol{\epsilon}^+(\mathbf{x}) = \frac{1}{2}(\nabla^T \mathbf{u}^+(\mathbf{x}) + \nabla \mathbf{u}^+(\mathbf{x})) \qquad \mathbf{x} \in \Omega^+ \tag{5}$$

$$\boldsymbol{\sigma}^-(\mathbf{x}) = \mathbf{C}^- : \boldsymbol{\epsilon}^-(\mathbf{x}) \qquad \mathbf{x} \in \Omega^- \qquad \boldsymbol{\epsilon}^-(\mathbf{x}) = \frac{1}{2}(\nabla^T \mathbf{u}^-(\mathbf{x}) + \nabla \mathbf{u}^-(\mathbf{x})) \qquad \mathbf{x} \in \Omega^- \tag{6}$$

where $\mathbf{C}^+$ and $\mathbf{C}^-$ are the stiffness tensors of the subdomains Ω^+ and Ω^- respectively. The displacement fields $\mathbf{u}^+$ and $\mathbf{u}^-$ are subsets of the kinematically admissible displacement field, $\mathbf{U}$:

$$\mathbf{u}^+ \in \mathbf{U} = \{\mathbf{v}^+ \in \mathbf{V} : \mathbf{v}^+ = \mathbf{0} \quad \mathbf{x} \in \Gamma_u^+\} \qquad \mathbf{u}^- \in \mathbf{U} = \{\mathbf{v}^- \in \mathbf{V} : \mathbf{v}^- = \mathbf{0} \quad \mathbf{x} \in \Gamma_u^-\} \tag{7}$$

Equations (1)-(7) can be converted into a weak form using the principle of virtual work. Its application to the two subdomains Ω^+ and Ω^- leads to

$$\int_{\Omega^+} \boldsymbol{\sigma}^+(\mathbf{x}) : \boldsymbol{\epsilon}^+(\mathbf{v}^+(\mathbf{x}))d\Omega = \int_{\Gamma_t^+} \mathbf{t}_{\mathbf{ext}}^+(\mathbf{x}).\mathbf{v}^+(\mathbf{x})d\Gamma + \int_{\Gamma_c} \mathbf{t}_{\mathbf{int}}^+(\mathbf{x}).\mathbf{v}^+(\mathbf{x})d\Gamma \qquad \forall \mathbf{v} \in \mathbf{U} \tag{8}$$

$$\int_{\Omega^-} \boldsymbol{\sigma}^-(\mathbf{x}) : \boldsymbol{\epsilon}^-(\mathbf{v}^-(\mathbf{x}))d\Omega = \int_{\Gamma_t^-} \mathbf{t}_{\mathbf{ext}}^-(\mathbf{x}).\mathbf{v}^-(\mathbf{x})d\Gamma + \int_{\Gamma_c} \mathbf{t}_{\mathbf{int}}^-(\mathbf{x}).\mathbf{v}^-(\mathbf{x})d\Gamma \qquad \forall \mathbf{v} \in \mathbf{U} \tag{9}$$

The left-hand sides of equations (8) and (9) are the internal virtual work, the right-hand sides are the virtual work carried out by the external forces and the tractions along the weak discontinuity surface. The existence of a weak discontinuity surface translates into the following conditions:

$$\mathbf{u}^+(\mathbf{x}) = \mathbf{u}^-(\mathbf{x}) \quad \mathbf{x} \in \Gamma_c \tag{10}$$

$$\mathbf{t}^+(\mathbf{x}) = -\mathbf{t}^-(\mathbf{x}) \quad \mathbf{x} \in \Gamma_c \tag{11}$$

The subdomains Ω^+ and Ω^- are now discretized with finite elements. Let $\{d^+\}$ and $\{d^-\}$ be the vectors of degrees of freedom of Ω^+ and Ω^- respectively. The displacement field in each sub-domain is obtained thanks to standard FE shape function matrices $[N^+]$ and $[N^-]$:

$$\mathbf{u}^+(\mathbf{x}) = [N^+(\mathbf{x})]\{d^+\} \qquad \mathbf{x} \in \Omega^+ \qquad \mathbf{u}^-(\mathbf{x}) = [N^-(\mathbf{x})]\{d^-\} \qquad \mathbf{x} \in \Omega^- \tag{12}$$

These shape functions are expressed as if the weak discontinuity surfaces were defined from the onset of the numerical calculation using a conforming mesh. Substitution of (12) into the weak forms (8) and (9), followed by the standard Bubnov–Galerkin approach, leads to the discretized equilibrium equations

$$[L^+]\{d^+\} = \begin{Bmatrix} fext^+ \\ fweak^+ \end{Bmatrix} \qquad [L^-]\{d^-\} = \begin{Bmatrix} fext^- \\ fweak^- \end{Bmatrix} \tag{13}$$

where $[L^+]$ and $[L^-]$ are the stiffness matrices of the two subdomains, $\{fext^+\}$ and $\{fext^-\}$ are the external force vectors induced by the external tractions and $\{fweak^+\}$ and $\{fweak^-\}$ are the equivalent force vectors induced by the tractions on the

weak discontinuity surface such that

$$[L^+] = \int_{\Omega^+} [B^+(\mathbf{x})]^t [\mathbf{C}^+][B^+(\mathbf{x})] d\Omega \qquad [L^-] = \int_{\Omega^-} [B^-(\mathbf{x})]^t [\mathbf{C}^-][B^-(\mathbf{x})] d\Omega \tag{14}$$

$$\{fext^+\} = \int_{\Gamma_t^+} [N^+(\mathbf{x})] \mathbf{t}^+_{\mathbf{ext}}(\mathbf{x}) d\Gamma \qquad \{fext^-\} = \int_{\Gamma_t^-} [N^-(\mathbf{x})] \mathbf{t}^-_{\mathbf{ext}} d\Gamma \tag{15}$$

$$\{fweak^+\} = \int_{\Gamma_c} [N^+(\mathbf{x})] \mathbf{t}^+_{\mathbf{int}}(\mathbf{x}) d\Gamma \qquad \{fweak^-\} = \int_{\Gamma_c} [N^-(\mathbf{x})] \mathbf{t}^-_{\mathbf{int}}(\mathbf{x}) d\Gamma \tag{16}$$

Equation (14) introduces the strain-displacement matrices, $[B^+]$ and $[B^-]$, which contain the derivatives of the classical FE shape functions (see, *e.g.*,[48] section 2.5). The degrees of freedom vectors in (13) are further partitioned between those associated with the weak discontinuity surface (called $\{dweak^+\}$ and $\{dweak^-\}$) and those associated with the bulk (called $\{dext^+\}$ and $\{dext^-\}$).

$$\{d^+\} = \begin{Bmatrix} dext^+ \\ dweak^+ \end{Bmatrix} \qquad \{d^-\} = \begin{Bmatrix} dext^- \\ dweak^- \end{Bmatrix} \tag{17}$$

This partition is used to rewrite (13) the following way:

$$\begin{bmatrix} L_{11^+} & L_{12^+} \\ L_{21^+} & L_{22^+} \end{bmatrix} \begin{Bmatrix} dext^+ \\ dweak^+ \end{Bmatrix} = \begin{Bmatrix} fext^+ \\ fweak^+ \end{Bmatrix} \qquad \begin{bmatrix} L_{11^-} & L_{12^-} \\ L_{21^-} & L_{22^-} \end{bmatrix} \begin{Bmatrix} dext^- \\ dweak^- \end{Bmatrix} = \begin{Bmatrix} fext^- \\ fweak^- \end{Bmatrix} \tag{18}$$

Relations (10), (11), (12) and (16) lead to

$$\{fweak^+\} = -\{fweak^-\} \qquad \{dweak^+\} = \{dweak^-\} \tag{19}$$

Substitution of (19) into (18) allows to eliminate $\{dweak^+\}$ and $\{dweak^-\}$ from the the discretized equilibrium equations. The resulting relation is called the condensed discretized equilibrium equation and reads

$$\{fext\} = \begin{bmatrix} L^-_{11} - L_{12^-}\Lambda^{-1}L_{21^-} & -L_{12^-}\Lambda^{-1}L_{21^+} \\ -L_{12^+}\Lambda^{-1}L_{21^-} & L^+_{11} - L_{12^+}\Lambda^{-1}L_{21^+} \end{bmatrix} \{dext\} \tag{20}$$

where

$$\{dext\} = \begin{Bmatrix} dext^- \\ dext^+ \end{Bmatrix} \qquad \{fext\} = \begin{Bmatrix} fext^- \\ fext^+ \end{Bmatrix} \tag{21}$$

and:

$$[\Lambda] = [L_{22^+}] + [L_{22^-}] \tag{22}$$

Equation (20) introduces the stiffness matrix of the augmented finite elements. The element stiffness matrices are assembled to form the global matrix of the system. Since $\{dweak^+\}$ and $\{dweak^-\}$ do not appear in the condensed discretized equilibrium equation (20), the nodes associated with these DOF, called internal nodes (see Figure 3) do not contribute to the size of the global stiffness matrix. Once $\{dext\}$ is known, $\{dweak^+\}$ and $\{dweak^-\}$ can be readily determined. Indeed, equations (18) and (19) lead to:

$$\{dweak^+\} = \{dweak^-\} = -[\Lambda]^{-1}\left([L_{21^+}]\{dext^+\} + [L_{21^-}]\{dext^-\}\right) \tag{23}$$

As highlighted by Equation (12), the AFEM and the classical FEM make use of the same shape functions to describe the displacement field on both sides of a weak discontinuity. This is illustrated in Figure 4 where a discontinuity crosses a triangular domain. The main difference between the FEM and the AFEM lies in the fact that the internal nodes (see Figure 3) are condensed at the element level with the AFEM. As a result, the DOF associated with these internal nodes are absent from the discretized equilibrium equation (20). The internal nodes should be thought as internal variables associated with a given element rather than conventional nodes shared between several elements. Hence, the AFEM can model an arbitrary number of (possibly moving) weak discontinuities without modifying the number of DOF per element or the size of the assembled stiffness matrix. This attractive property, not shared by the FEM or the XFEM, comes at a price: since the internal nodes are condensed at the element level, the interelement compatibility is lost.

3.2 | Application to the 2D linear elements of this study

The condensed discretized equilibrium equation (20) can be used with parent elements of any dimension and order. Particularization to 2D elements with linear shape functions is considered next. The parent elements used in this study are the constant strain triangle, called hereafter T3, and the bilinear quadrilateral called Q4. A weak discontinuity splits a T3 into a triangle and a quadrangle, the resulting element is called an AT3. When a Q4 is augmented, two situations can occur depending on the location of the discontinuity: *i)* it is split into two quadrangles and the resulting element is named AQ4-1 or *ii)* it is split into a triangle and a pentagon, the resulting element is called AQ4-2, see Figure 3. As stated in the introduction, the most salient feature of the AFEM is that augmented elements and their parent elements share the same degrees of freedom, see Table 1. For instance, the AT3 has the same DOF as a T3, despite the fact that the former embeds a weak discontinuity, as illustrated in Figure 4.

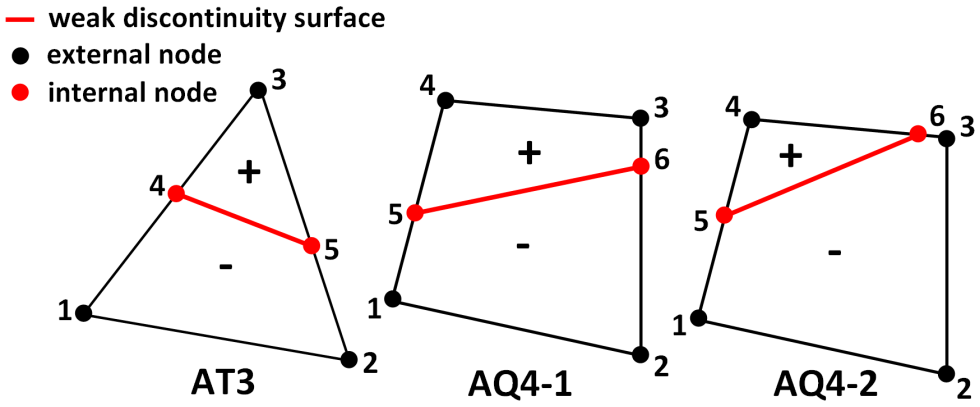

FIGURE 3 Node numbering of the augmented elements used in this study

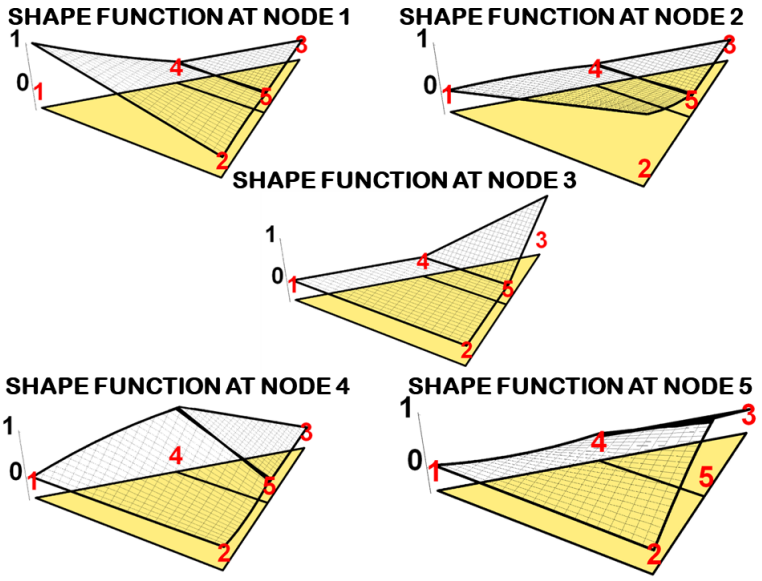

FIGURE 4 Shape functions associated with the internal and external nodes of an AT3 element

The shape functions of the Q4 and the T3 can be found in classical textbooks on the finite element method see, e.g.,[48]. The stiffness matrices of quadrilateral and triangular (sub)domains are computed thanks to a 2×2 points Gauss integration scheme

and a 1-point integration scheme respectively. Pentagonal elements, called P5, are implemented using the polygonal finite element method proposed by Sukumar and co-workers [52,53,54]. A 6-point integration scheme has been used to evaluate the stiffness matrices of the P5 used in this study.

TABLE 1 Degrees of freedom of the augmented elements used in this study

Augmented Element	$\{dext\}^t$	$\{dweak\}^t$ (condensed DOF)
AT3	$\{u_1, v_1, u_2, v_2, u_3, v_3\}$	$\{u_4, v_4, u_5, v_5\}$
AQ4-1	$\{u_1, v_1, u_2, v_2, u_3, v_3, u_4, v_4\}$	$\{u_5, v_5, u_6, v_6\}$
AQ4-2	$\{u_1, v_1, u_2, v_2, u_3, v_3, u_4, v_4\}$	$\{u_5, v_5, u_6, v_6\}$

4 | THE BIMATERIAL BOUNDARY VALUE PROBLEM

4.1 | Problem description

To investigate the performances of the AFEM we resort to a problem often encountered in the XFEM literature called the bimaterial boundary value problem [55,23,56,15,57,31]. Let us consider a circular body composed of two different materials Ω_1 and Ω_2 as depicted in Figure 5. The radius of Ω_1 is $a = 0.4$ while the radius of Ω_2 is $b = 2.0$. The material properties in Ω_1 are: $E_1 = 1$, $\nu_1 = 0.25$, and those in Ω_2 are: $E_2 = 10$, $\nu_2 = 0.3$. The corresponding Lamé coefficients are: $\lambda_1 = \mu_1 = 0.4$ and $\lambda_2 = 5.7692$, $\mu_2 = 3.8461$. This set of material properties will be called *soft inclusion* hereafter. The two materials are perfectly bonded and we assume plane strain conditions. The size of the domain, the material parameters and the radial loading are the same as the one considered by Sukumar *et al.* [55]. The following displacement field is imposed on the boundary Γ of the domain:

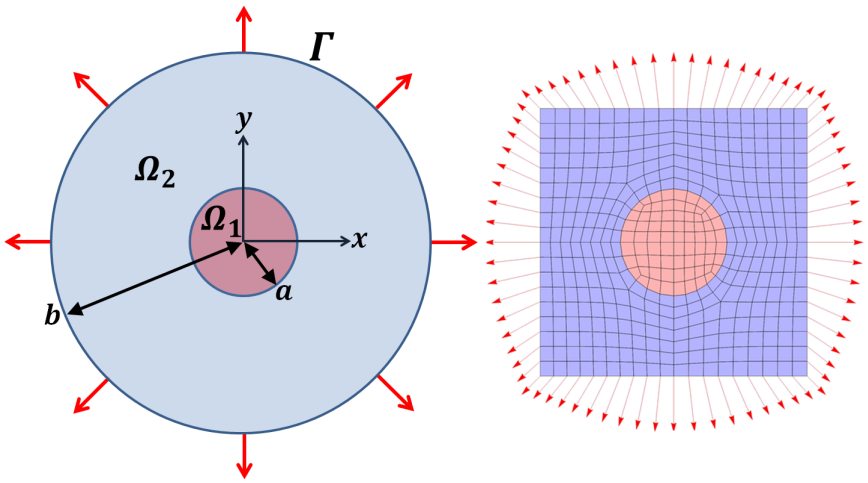

FIGURE 5 Bimaterial boundary value problem (left) and associated numerical model (right)

$$\begin{cases} u_r(r = b, \theta) = b \\ u_\theta(r = b, \theta) = 0 \end{cases} \tag{24}$$

The closed-form solution provided in[55] in polar coordinates is recalled:

$$u_r(r,\theta) = \begin{cases} \left((1-\frac{b^2}{a^2})\alpha + \frac{b^2}{a^2}\right) r & 0 \le r \le a \\ (r-\frac{b^2}{r})\alpha + \frac{b^2}{r} & a \le r \le b \end{cases} \tag{25}$$

$$u_\theta(r,\theta) = 0 \tag{26}$$

where:

$$\alpha = \frac{(\lambda_1+\mu_1+\mu_2)b^2}{(\lambda_2+\mu_2)a^2 + (\lambda_1+\mu_1)(b^2-a^2) + \mu_2 b^2} \tag{27}$$

The exact strain field reads:

$$\epsilon_{rr}(r,\theta) = \begin{cases} (1-\frac{b^2}{a^2})\alpha + \frac{b^2}{a^2} & 0 \le r \le a \\ (1+\frac{b^2}{r^2})\alpha - \frac{b^2}{r^2} & a \le r \le b \end{cases} \tag{28}$$

$$\epsilon_{\theta\theta}(r,\theta) = \begin{cases} (1-\frac{b^2}{a^2})\alpha + \frac{b^2}{a^2} & 0 \le r \le a \\ (1-\frac{b^2}{r^2})\alpha + \frac{b^2}{r^2} & a \le r \le b \end{cases} \tag{29}$$

$$\epsilon_{r\theta}(r,\theta) = 0 \tag{30}$$

In the numerical model we consider a square plate with a side length $L = 2$. The exact displacement field is imposed on the boundary of this plate (see Figure 5). To assess the convergence rate of the numerical methods we evaluate the error in the energy norm, it is defined as follows:

$$||e|| = \left(\int_\Omega (\epsilon - \hat{\epsilon}) : C : (\epsilon - \hat{\epsilon})\, d\Omega \right)^{\frac{1}{2}} \tag{31}$$

where: $\Omega = \Omega_1 \cup \Omega_2$, ϵ is the exact strain field, $\hat{\epsilon}$ is the strain field obtained thanks to the numerical methods and C is the elasticity tensor. We also define the relative energy norm error percentage as:

$$||\eta|| = 100\% \times \left(\frac{\int_\Omega (\epsilon - \hat{\epsilon}) : C : (\epsilon - \hat{\epsilon})\, d\Omega}{\int_\Omega \epsilon : C : \epsilon\, d\Omega} \right)^{\frac{1}{2}} \tag{32}$$

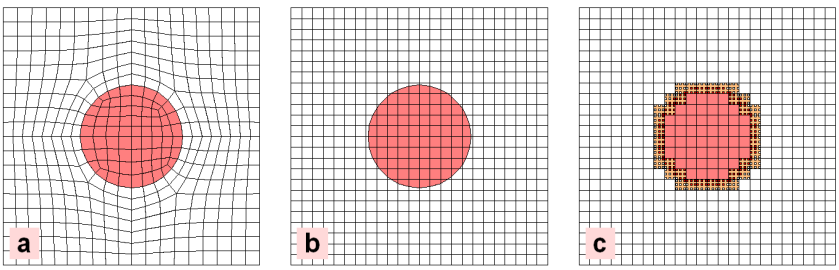

FIGURE 6 Numerical methods benchmarked in this study: a) the FEM with a mesh conforming to the discontinuity, b) the AFEM, c) the non-conforming FEM (the colour of the dots corresponds to the material properties used at the integration points of the elements)

4.2 | Numerical results and discussions

The performances of the AFEM are investigated and compared with two numerical methods: the classical FEM where the mesh conforms to the material interface (see Figure 6a) and the so-called non-conforming FEM (see Figure 6c). The comparisons are drawn for triangular and quadrilateral elements. The evolution of the relative energy norm error $||\eta||$ with the element size h is plotted in Figure 7. The optimal convergence rate of linear FEs in the energy norm is known to be 1[58]. It can be observed in

Figure 7 that this theoretical rate is indeed reached by standard FEs (*i.e.*, the elements denoted T3 and Q4). The convergence rate of the non-conforming FEM is approximately 0.5 which is in accordance with previously reported results[23,31]. The AFEM converges monotonically at the same rate. To gain further insight on these results, the spatial distribution of energy error is

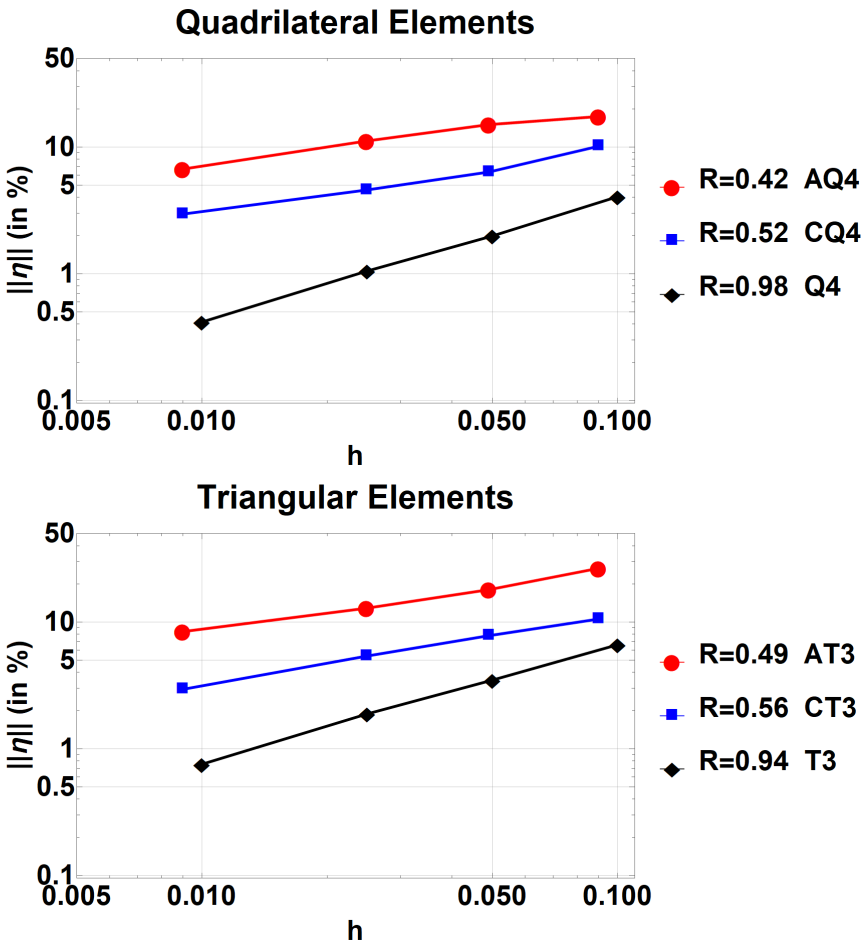

FIGURE 7 Rate of convergence in the energy norm for the bimaterial problem with the *soft inclusion* material properties: $E_1 = 1$, $\nu_1 = 0.25$, $E_2 = 10$, $\nu_2 = 0.3$

depicted in Figure 8 for the meshes with quadrilateral elements of size *h=0.05*. As expected, the highest error levels are located at the vicinity of the interface where the strain gradients are maximum. In this zone, the error induced by the AFEM is higher than the one of the FEM and the non-conforming FEM. The latter nevertheless introduces a larger pollution error in the inclusion where the expected constant strain field is poorly approximated. It also appears that the FEM outperforms the non-conforming FEM and the AFEM everywhere in the domain. The previous observations hold true with other element sizes, as well as with triangular elements. The sole results depicted in Figure 7 would suggest that the non-conforming FEM is more accurate than the AFEM. This assertion actually depends on the stiffness ratio between the inclusion and the matrix. Indeed, the poor ability of the non-conforming FEM to model the constant strain in the inclusion makes it less efficient than the AFEM if a stiffer inclusion is modelled. To illustrate this point, the bimaterial boundary value problem is repeated with the following material properties: $E_1 = 200$, $\nu_1 = 0.25$ in Ω_1 and $E_2 = 1$, $\nu_2 = 0.3$ in Ω_2. Such a stiffness contrast is typical of carbon fibre reinforced plastics see, *e.g.*,[59]. This set of material properties will be called *hard inclusion* hereafter. With these material properties the AFEM performs better than the non-conforming FEM, see Figure 9. We also notice that the use of the non-conforming FEM now induces higher error levels than the FEM and the AFEM, not only in the inclusion but also in the rest of the domain, see Figure 10.

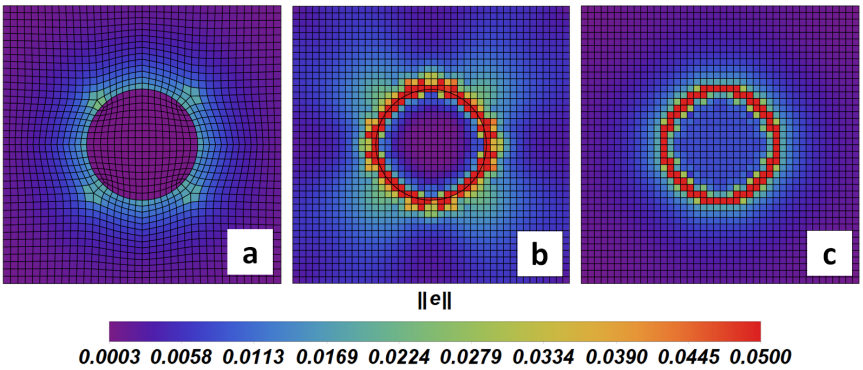

FIGURE 8 Error in the energy norm for quadrilateral meshes of size $h = 0.05$ with the *soft inclusion* material properties: $E_1 = 1$, $\nu_1 = 0.25$, $E_2 = 10$, $\nu_2 = 0.3$, a) FEM (with Q4 elements), b) AFEM (with AQ4 elements), c) non-conforming FEM (with CQ4 elements)

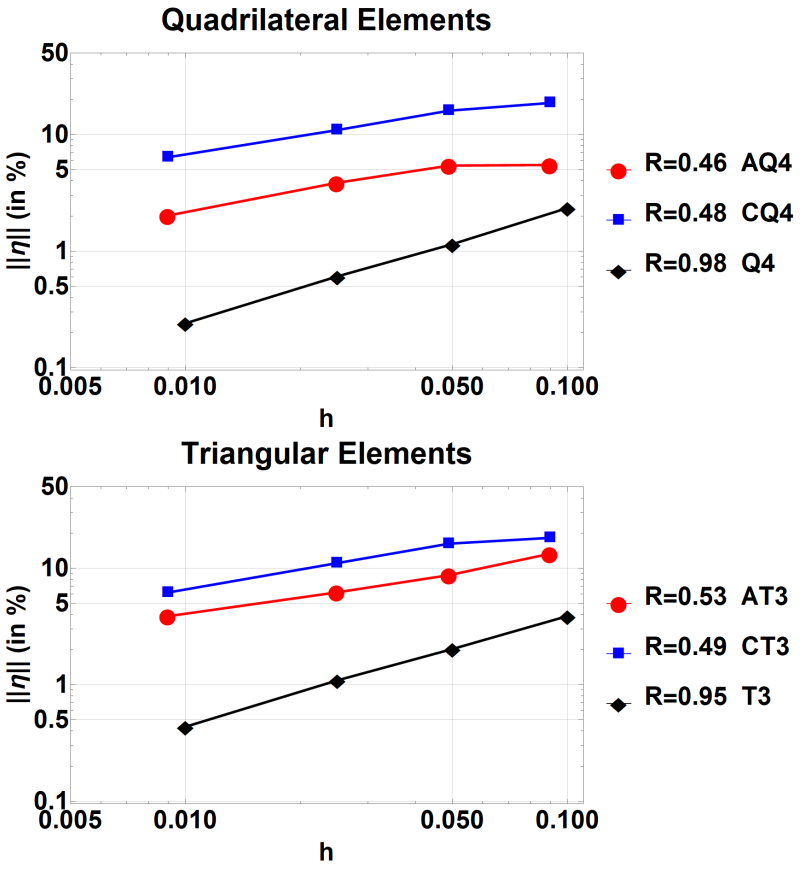

FIGURE 9 Rate of convergence in the energy norm for the bimaterial problem with the *hard inclusion* material properties: $E_1 = 200$, $\nu_1 = 0.25$, $E_2 = 1$, $\nu_2 = 0.3$

5 | EFFECTIVE STIFFNESS OF HETEROGENEOUS MATERIALS

Depending on the quantity of interest, one may accept a moderate error on the local field, as long as the effective properties fall within the expected accuracy. Thus, in this next numerical setup we now examine an homogenization problem.

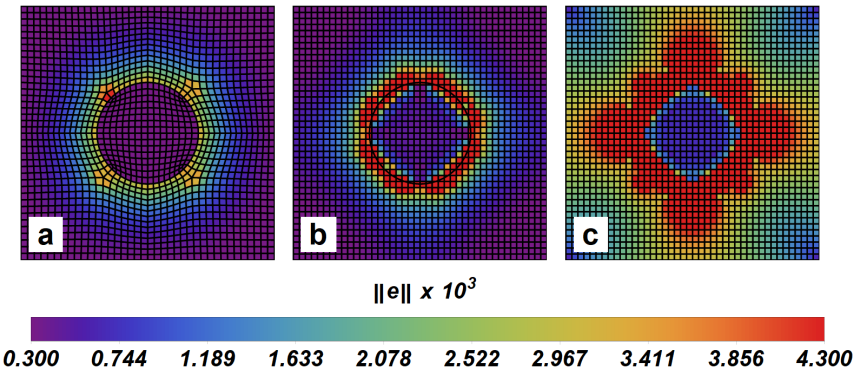

FIGURE 10 Error in the energy norm for quadrilateral meshes of size $h = 0.05$ and the *hard inclusion* material properties: $E_1 = 200$, $\nu_1 = 0.25$, $E_2 = 1$, $\nu_2 = 0.3$: a) FEM (with Q4 elements), b) AFEM (with AQ4 elements), c) non-conforming FEM (with CQ4 elements)

5.1 | Problem description

Numerical homogenization is a way to derive the macroscopic properties of heterogeneous materials based on computations performed at the microscopic scale. While several quantities can be extracted from the microscopic computations, the reaction forces on the boundary of the microscopic cell may suffice to derive its effective macroscopic properties[60]. To investigate the performances of the AFEM, we thus submit a square cell comprising seven inclusions to a simple shear loading and measure the associated reaction force. Comparisons are drawn for triangular and quadrilateral elements. Dirichlet boundary conditions are used to generate the loading. Let $u(x, y)$ and $v(x, y)$ be the displacement fields in directions x and y respectively, the boundary conditions write: $u(x = 0) = v(x = 0) = u(x = L) = 0$ and $v(x = L) = 1$, see Figure 11. The side length of the square domain

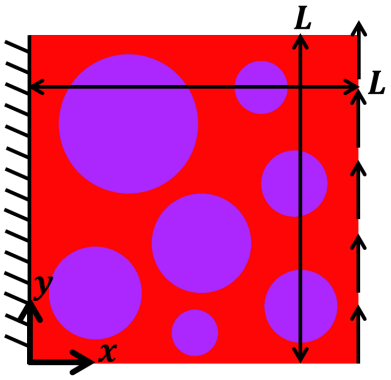

FIGURE 11 Microscopic cell clamped on one side and submitted to a vertical displacement on the other side

is $L = 10$ and plane strain conditions are assumed. The material properties of the inclusions and the surrounding material are: $E_1 = 10$, $\nu_1 = 0.2$ and $E_2 = 1$, $\nu_2 = 0.3$ respectively. This set of material properties will be called *hard inclusion* hereafter. The locations of the inclusions as well as their radius are given in Table 2. The accuracy of the AFEM is compared to those of the FEM and the non-conforming FEM. To illustrate the use of these strategies, the shear strain field obtained with meshes comprising approximately the same number of degrees of freedom is plotted in Figure 12. The relative error in reaction force is used to compare the numerical methods mentioned above. It is defined as follows:

$$||e|| = 100\% \times \frac{\widehat{f_{reaction}} - f_{reaction}}{f_{reaction}} \tag{33}$$

TABLE 2 Location and radius of the inclusions

inclusion	coordinates of the center {x,y}	radius
1	{5.2, 3.7}	1.5
2	{8.0, 5.5}	1.0
3	{2.0, 2.2}	1.4
4	{8.2, 1.8}	1.1
5	{5.0, 1.0}	0.7
6	{3.0, 7.3}	2.1
7	{7.0, 8.4}	0.8

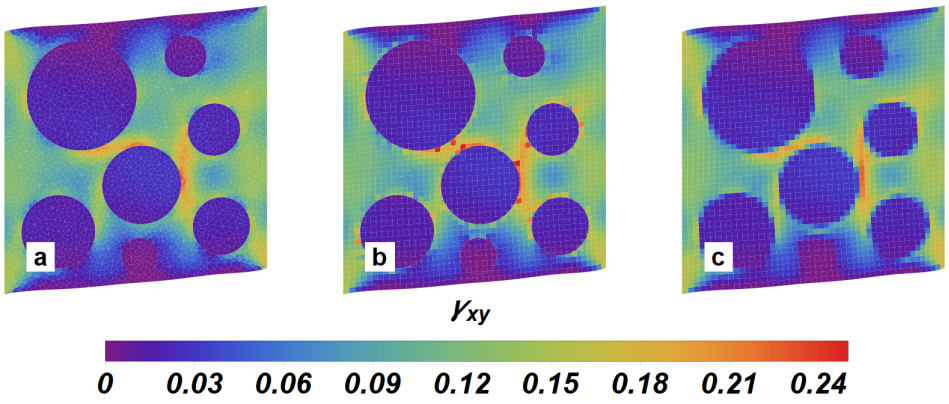

FIGURE 12 Shear strain field within the microscopic cell with the *hard inclusion* material properties: a) FEM (6798 DOF), b) AFEM (5000 DOF) and c) non-conforming FEM (5000 DOF)

where $f_{reaction}$ is the exact reaction force and $\widehat{f_{reaction}}$ is the reaction force obtained with the numerical methods. The "exact" reaction force is estimated using an overrefined Q4 mesh with 7 million degrees of freedom.

5.2 | Numerical results and discussions

The evolution of the relative error in reaction force with mesh refinement is plotted in Figure 13. The AFEM ability to obtain the exact reaction force is notably influenced by the choice of the parent element, *i.e.*, triangular or quadrilateral, which departs from the observations made in the previous section: the use of augmented triangular or quadrilateral elements provided similar error levels in the energy norm for a given element size (see Figure 7 and 9). The example investigated here emphasizes the superior accuracy of the AQ4 over the AT3. The solutions obtained with the AFEM appears to be softer than the exact solution, *i.e.*, the reaction forces are systematically underestimated when the microstructure is submitted to a given displacement. This differs from the FEM which is proven to overestimate the stiffness see, *e.g.*,[48] p.188. The microstructures modelled with the non-conforming FEM are also overly stiff and the associated results are systematically less accurate than those obtained with the FEM or the AFEM. One also notices that the FEM outperforms the AFEM when triangular elements are considered but this is no longer the case with quadrilateral elements where the AFEM predictions are on par with the FEM results, see Figure 13. As revealed in the previous section, the relative performances of the AFEM and the non-conforming FEM depend on the ratio of material properties at the weak discontinuity. For the comparisons to be complete, we thus repeated the microstructural problem with the following properties: $E_1 = 1$, $\nu_1 = 0.2$ and $E_2 = 10$, $\nu_2 = 0.3$ respectively. This set of material properties is called *soft inclusion*. The AFEM is now observed to be moderately less accurate than the non-conforming FEM, see Figure 14, and the latter appears to perform as well as the FEM in this case.

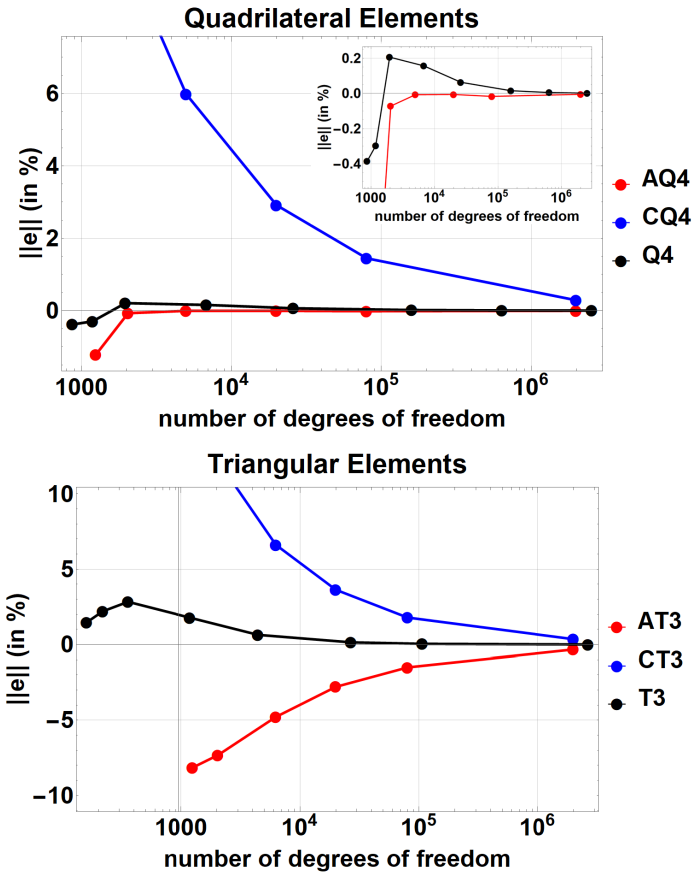

FIGURE 13 Evolution of the relative error in reaction force with mesh refinement with the *hard inclusion* material properties

6 | CONDITIONING ISSUES

The use of the XFEM to model weak or strong discontinuities may result in a poor conditioning of the linear system of equations to be solved. Indeed, the condition number of XFEM matrices deteriorates severely as discontinuities get close to a node, see, *e.g.*,[22]. As a result, tackling XFEM problems with iterative solvers imposes to use both classical preconditioners (such as incomplete LU) and XFEM-tailored ones[61,22]. The aim of this section is to assess how sensitive is the AFEM to the position of a weak discontinuity within an element. To do so, condition numbers of stiffness matrices arising from the use of the AFEM are compared with those obtained with the FEM.

6.1 | Problem description

The numerical experiments presented in this section are inspired from the ones performed in[22]. A triangular domain that embeds a weak discontinuity is considered. The weak discontinuity splits the triangular domain into two elastic and isotropic domains : domain 1 whose material properties are E_1 and ν_1 and domain 2 with material properties E_2 and ν_2 , see Figure 15.

This situation is modelled with the standard FEM and the AFEM. The FEM mesh is made of 2 elements (a Q4 and a T3) and the resulting assembled stiffness matrix is 10×10. A single augmented triangular element (AT3) models the whole triangular domain, resulting in a 6×6 stiffness matrix. The position of the discontinuity is parametrised by the value $y_{discontinuity} \in]-1,+1[$. The values -1 and 1 are excluded from the interval since they would lead to the generation of a zero-volume element with the FEM and a zero-volume subdomain with the AFEM. One should simply use a classical triangular element (T3), embedding no weak discontinuity, to handle this situation with the aforementioned methods. The stiffness matrix obtained with the FEM, K_{FEM}, has three zero eigenvalues since three rigid body motions are possible. The same holds true for the AFEM stiffness matrices K_{AFEM}. In order to determine the condition number - κ - of these matrices, we compute their eigenvalues, rank them

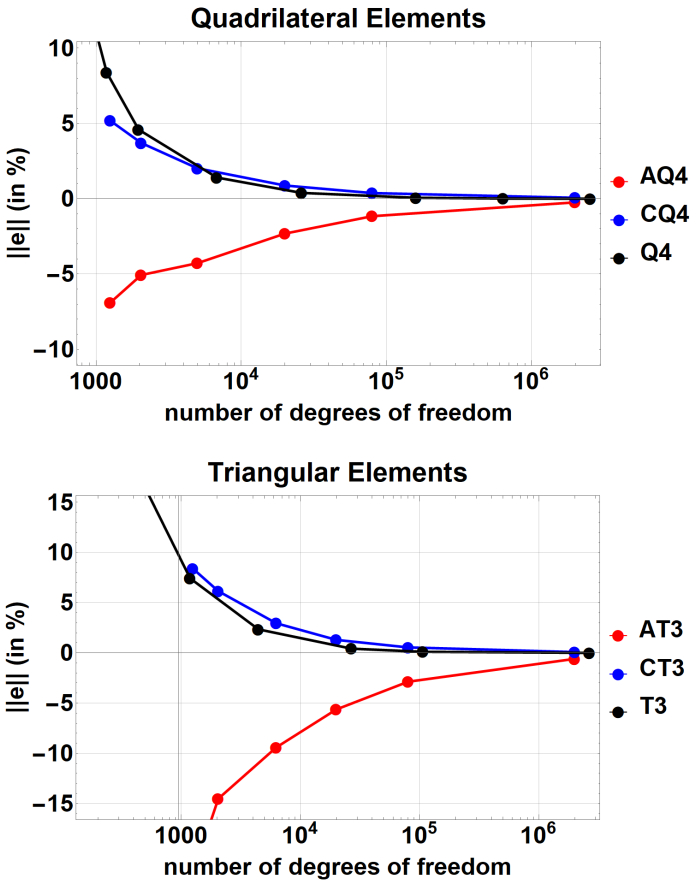

FIGURE 14 Evolution of the relative error in reaction force with mesh refinement with the *soft inclusion* material properties

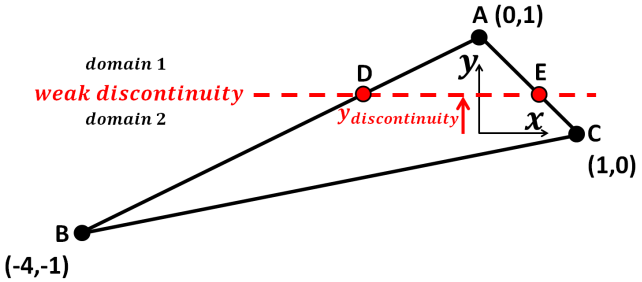

FIGURE 15 Triangular domain split by a weak discontinuity

in descending order and suppress the three expected zero eigenvalues. This is formally expressed by the following equations:

$$\kappa_{FEM} = \frac{1^{st}eigenvalue(K_{FEM})}{7^{th}eigenvalue(K_{FEM})} \qquad \kappa_{AFEM} = \frac{1^{st}eigenvalue(K_{AFEM})}{3^{rd}eigenvalue(K_{AFEM})} \tag{34}$$

6.2 | Numerical results and discussions

The evolution of the condition number with the position of the discontinuity are plotted in Figure 16. Two sets of material properties are investigated and we compare the results obtained with the FEM and the AFEM. The curves plotted in Figure 16 are discontinuous at $y_{discontinuity} = 0$. It corresponds to a change of the shape functions describing the displacement field on both sides of the weak discontinuity. Indeed, when $y_{discontinuity} > 0$, domains 1 and 2 are a triangle and a quadrilateral, respectively,

but it is the opposite as soon as $y_{discontinuity} < 0$. When $y_{discontinuity} = 0$, a degenerated element is created: the quadrilateral BCED becomes a triangle since nodes E and C are superimposed. No specific procedure was needed to handle this case and it does not severely deteriorate the condition numbers. The main result of these numerical experiments is that the condition number of AFEM matrices is systematically lower than the one of FEM matrices. Hence, there is no need to develop specific preconditioners in order to solve AFEM problems with iterative solvers.

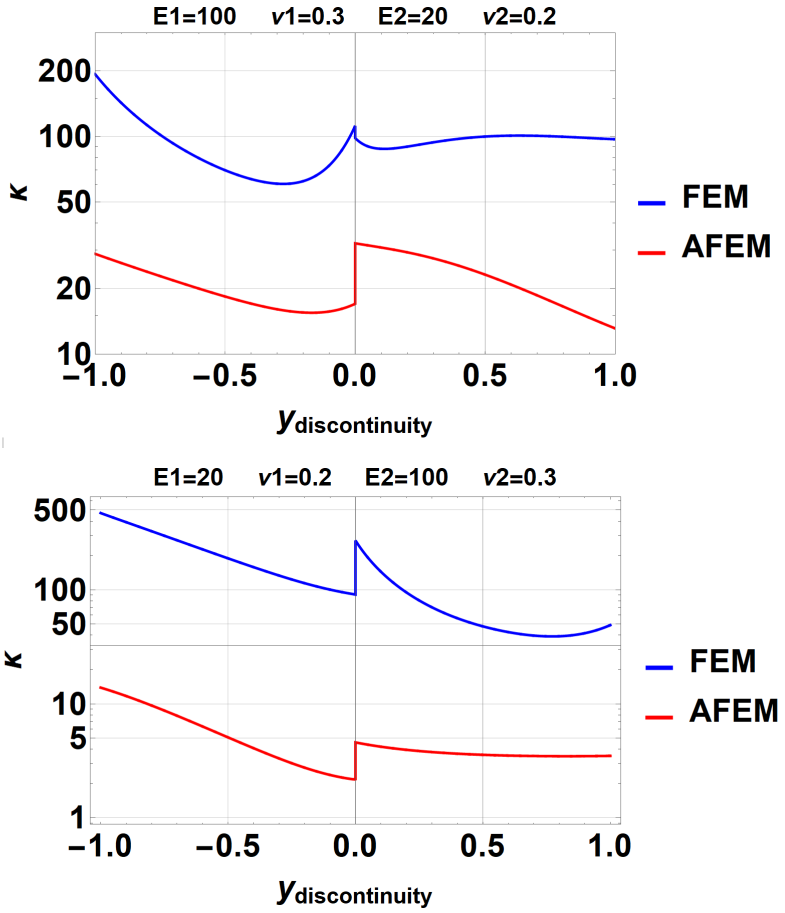

FIGURE 16 Evolution of the condition number with the position of the weak discontinuity, for two sets of material properties (each curve is made of two hundred thousand regularly-spaced points)

7 | CONCLUSIONS

The ability of the AFEM to model weak discontinuity surfaces in 2D has been thoroughly investigated. To make this investigation as complete as possible, triangular and quadrilateral elements were used, the ratio of elements sizes between the coarsest and the finest meshes was systematically greater than ten, the error in the energy norm as well as the error in reaction forces were considered and the contrast of material properties at the weak discontinuity was varied. The performances of the AFEM were compared with the ones of the non-conforming FEM and the FEM. The latter is known to be optimally convergent for the set of problems tackled in this study. The convergence rate of the AFEM in the energy norm was found to be suboptimal: $\mathcal{O}(h^{0.5})$ instead of $\mathcal{O}(h)$. Our study suggests that the observed loss of convergence is caused by the violation of the interelement compatibility induced by the use of augmented elements. Indeed, this incompatibility is the most significant difference between the FEM and the AFEM.

The non-conforming FEM shares the same convergence rate as the AFEM. One cannot claim superiority of one method over the other. Indeed, their relative performances are notably impacted by the stiffness ratio of the materials at the weak discontinuity. The non-conforming FEM was found to be more accurate than the AFEM if soft inclusions embedded in a harder matrix are modelled. On the other hand, the AFEM is of superior accuracy when stiff fibres surrounded by a softer matrix are modelled. A noticeable advantage of the AFEM over the non-conforming FEM is that it naturally allows to model the transition from a weak discontinuity to a strong one.

One of the most significant findings to emerge from this study is that augmented quadrilateral elements (AQ4) can provide results as accurate as the FEM in homogenization problems, see Figure 13. The AFEM thus enjoys the flexibility of the XFEM in dealing with discontinuities independently of the mesh while greatly lowering its complexity: it needs neither additional degrees of freedom nor blending elements and makes use of standard quadrature schemes.

In light of the observed levels of error in the energy norm at the vicinity of weak discontinuities, the ability of the AFEM to model non-linear interfacial phenomena is questionable. The AFEM has already been successfully used to simulate fibre–matrix interface debonding[36] but it is believed that these aspects deserve further investigations.

Possible extensions of the AFEM include the modelling of moving weak discontinuities such as encountered in Stefan problems. The AFEM is an ideal candidate to tackle these situations for at least two reasons: the imposition of boundary conditions on the interface is trivial (see equations (18) and (19)) and, thanks to the condensation process, the size of the system of linear equations is unaffected by the location and the number of weak discontinuities. Our study does not allow to rigorously estimate the convergence rate of the AFEM when applied to (time-dependent) Stefan problems since we have only considered (time-independent) elliptic partial differential equations (PDEs). Nevertheless, we believe that the same convergence rate as the one in this study should be observed, if the AFEM implementation follows the guidelines proposed by Belytschko and co-workers for the XFEM[62].

Author contributions

S. Essongue: Conceptualization (lead); Methodology (lead); Investigation (lead); Software (lead); Writing - Original Draft (lead); Writing - Review and Editing (equal). **G. Couégnat**: Conceptualization (supporting); Methodology (supporting); Software (supporting); Supervision (lead); Writing - Original Draft (supporting); Writing - Review and Editing (equal). **E. Martin**: Supervision (supporting); Writing - Original Draft (supporting); Writing - Review and Editing (equal).

Conflict of interest

The authors declare no potential conflict of interests.

References

1. Recht RF. Catastrophic Thermoplastic Shear. *Journal of Applied Mechanics* 1964; 31(2): 189–193. doi: 10.1115/1.3629585

2. Vogler T. Initiation and axial propagation of kink bands in fiber composites. *Acta Materialia* 1997; 45(6): 2443–2454. doi: 10.1016/S1359-6454(96)00350-3

3. Hill R. A general theory of uniqueness and stability in elastic-plastic solids. *Journal of the Mechanics and Physics of Solids* 1958; 6(3): 236–249. doi: 10.1016/0022-5096(58)90029-2

4. Rudnicki J, Rice J. Conditions for the localization of deformation in pressure-sensitive dilatant materials. *Journal of the Mechanics and Physics of Solids* 1975; 23(6): 371–394. doi: 10.1016/0022-5096(75)90001-0

5. Rizzi E, Carol I, Willam K. Localization Analysis of Elastic Degradation with Application to Scalar Damage. *Journal of Engineering Mechanics* 1995; 121(4): 541–554. doi: 10.1061/(ASCE)0733-9399(1995)121:4(541)

6. Bordas S, Moran B. Enriched finite elements and level sets for damage tolerance assessment of complex structures. *Engineering Fracture Mechanics* 2006; 73(9): 1176–1201. doi: 10.1016/j.engfracmech.2006.01.006

7. Belytschko T, Gracie R, Ventura G. A review of extended/generalized finite element methods for material modeling. *Modelling and Simulation in Materials Science and Engineering* 2009; 17(4): 043001. doi: 10.1088/0965-0393/17/4/043001

8. Wu JY. Unified analysis of enriched finite elements for modeling cohesive cracks. *Computer Methods in Applied Mechanics and Engineering* 2011; 200(45-46): 3031–3050. doi: 10.1016/j.cma.2011.05.008

9. Oliver J, Huespe A, Sánchez P. A comparative study on finite elements for capturing strong discontinuities: E-FEM vs X-FEM. *Computer Methods in Applied Mechanics and Engineering* 2006; 195(37-40): 4732–4752. doi: 10.1016/j.cma.2005.09.020

10. Costa D.-dD, Alfaiate J, Sluys LJ, Júlio E. A comparative study on the modelling of discontinuous fracture by means of enriched nodal and element techniques and interface elements. *International Journal of Fracture* 2010; 161(1): 97–119. doi: 10.1007/s10704-009-9432-6

11. Belytschko T, Black T. Elastic crack growth in finite elements with minimal remeshing. *International Journal for Numerical Methods in Engineering* 1999; 45(5): 601–620. _eprint: https://onlinelibrary.wiley.com/doi/pdf/10.1002/%28SICI%291097-0207%2819990620%2945%3A5%3C601%3A%3AAID-NME598%3E3.0.CO%3B2-Sdoi: 10.1002/(SICI)1097-0207(19990620)45:5<601::AID-NME598>3.0.CO;2-S

12. Moës N, Dolbow J, Belytschko T. A finite element method for crack growth without remeshing. *International Journal for Numerical Methods in Engineering* 1999; 46(1): 131–150. doi: 10.1002/(SICI)1097-0207(19990910)46:1<131::AID-NME726>3.0.CO;2-J

13. C. A.M. Duarte IB. Generalized Finite Element Methods for Three Dimensional Structural Mechanics Problems. *Computers & Structures* 2000; 77(2): 215–232. doi: 10.1016/S0045-7949(99)00211-4

14. Strouboulis T, Copps K, Babuška I. The generalized finite element method. *Computer Methods in Applied Mechanics and Engineering* 2001; 190(32-33): 4081–4193. doi: 10.1016/S0045-7825(01)00188-8

15. Hansbo A, Hansbo P. A finite element method for the simulation of strong and weak discontinuities in solid mechanics. *Computer Methods in Applied Mechanics and Engineering* 2004; 193(33-35): 3523–3540. doi: 10.1016/j.cma.2003.12.041

16. Mergheim J, Kuhl E, Steinmann P. A finite element method for the computational modelling of cohesive cracks. *International Journal for Numerical Methods in Engineering* 2005; 63(2): 276–289. doi: 10.1002/nme.1286

17. Song JH, Areias PMA, Belytschko T. A method for dynamic crack and shear band propagation with phantom nodes. *International Journal for Numerical Methods in Engineering* 2006; 67(6): 868–893. doi: 10.1002/nme.1652

18. Melenk JM, Babuška I. The partition of unity finite element method: Basic theory and applications. *Computer Methods in Applied Mechanics and Engineering* 1996; 139(1–4): 289–314. doi: 10.1016/S0045-7825(96)01087-0

19. Babuška I, Melenk JM. The Partition of Unity Method. *International Journal for Numerical Methods in Engineering* 1997; 40(4): 727–758. _eprint: https://onlinelibrary.wiley.com/doi/pdf/10.1002/%28SICI%291097-0207%2819970228%2940%3A4%3C727%3A%3AAID-NME86%3E3.0.CO%3B2-Ndoi: 10.1002/(SICI)1097-0207(19970228)40:4<727::AID-NME86>3.0.CO;2-N

20. Areias PM, Belytschko T. A comment on the article "A finite element method for simulation of strong and weak discontinuities in solid mechanics" by A. Hansbo and P. Hansbo [Comput. Methods Appl. Mech. Engrg. 193 (2004) 3523–3540]. *Computer Methods in Applied Mechanics and Engineering* 2006; 195(9-12): 1275–1276. doi: 10.1016/j.cma.2005.03.006

21. Sukumar N, Dolbow JE, Moës N. Extended finite element method in computational fracture mechanics: a retrospective examination. *International Journal of Fracture* 2015; 196(1-2): 189–206. doi: 10.1007/s10704-015-0064-8

22. Ndeffo M, Massin P, Moës N, Martin A, Gopalakrishnan S. On the construction of approximation space to model discontinuities and cracks with linear and quadratic extended finite elements. *Advanced Modeling and Simulation in Engineering Sciences* 2017; 4(1). doi: 10.1186/s40323-017-0090-3

23. Moës N, Cloirec M, Cartraud P, Remacle JF. A computational approach to handle complex microstructure geometries. *Computer Methods in Applied Mechanics and Engineering* 2003; 192(28-30): 3163–3177. doi: 10.1016/S0045-7825(03)00346-3

24. Dvorkin EN, Cuitiño AM, Gioia G. Finite elements with displacement interpolated embedded localization lines insensitive to mesh size and distortions. *International Journal for Numerical Methods in Engineering* 1990; 30(3): 541–564. _eprint: https://onlinelibrary.wiley.com/doi/pdf/10.1002/nme.1620300311doi: 10.1002/nme.1620300311

25. Simo JC, Oliver J, Armero F. An analysis of strong discontinuities induced by strain-softening in rate-independent inelastic solids. *Computational Mechanics* 1993; 12(5): 277–296. doi: 10.1007/BF00372173

26. Jirásek M. Comparative study on finite elements with embedded discontinuities. *Computer Methods in Applied Mechanics and Engineering* 2000; 188(1): 307–330. doi: 10.1016/S0045-7825(99)00154-1

27. Borst dR, Wells G, Sluys L. Some observations on embedded discontinuity models. *Engineering Computations* 2001; 18(1/2): 241–254. doi: 10.1108/02644400110365897

28. Linder C, Armero F. Finite elements with embedded strong discontinuities for the modeling of failure in solids. *International Journal for Numerical Methods in Engineering* 2007; 72(12): 1391–1433. doi: 10.1002/nme.2042

29. Dujc J, Brank B, Ibrahimbegovic A. Stress-hybrid quadrilateral finite element with embedded strong discontinuity for failure analysis of plane stress solids. *International Journal for Numerical Methods in Engineering* 2013; 94(12): 1075–1098. _eprint: https://onlinelibrary.wiley.com/doi/pdf/10.1002/nme.4475doi: 10.1002/nme.4475

30. Babuška I. The finite element method for elliptic equations with discontinuous coefficients. *Computing* 1970; 5(3): 207–213. doi: 10.1007/BF02248021

31. Lian WD, Legrain G, Cartraud P. Image-based computational homogenization and localization: comparison between X-FEM/levelset and voxel-based approaches. *Computational Mechanics* 2013; 51(3): 279–293. doi: 10.1007/s00466-012-0723-9

32. Woo K, Whitcomb JD. Macro finite element using subdomain integration. *Communications in Numerical Methods in Engineering* 1993; 9(12): 937–949. doi: 10.1002/cnm.1640091202

33. Parvizian J, Düster A, Rank E. Finite cell method: h- and p-extension for embedded domain problems in solid mechanics. *Computational Mechanics* 2007; 41(1): 121–133. doi: 10.1007/s00466-007-0173-y

34. Düster A, Parvizian J, Yang Z, Rank E. The finite cell method for three-dimensional problems of solid mechanics. *Computer Methods in Applied Mechanics and Engineering* 2008; 197(45-48): 3768–3782. doi: 10.1016/j.cma.2008.02.036

35. Belytschko T, Fish J, Engelmann BE. A finite element with embedded localization zones. *Computer Methods in Applied Mechanics and Engineering* 1988; 70(1): 59–89. doi: 10.1016/0045-7825(88)90180-6

36. Liu W, Yang QD, Mohammadizadeh S, Su XY. An efficient augmented finite element method for arbitrary cracking and crack interaction in solids. *International Journal for Numerical Methods in Engineering* 2014; 99(6): 438–468. _eprint: https://onlinelibrary.wiley.com/doi/pdf/10.1002/nme.4697doi: 10.1002/nme.4697

37. Roubin E, Vallade A, Benkemoun N, Colliat JB. Multi-scale failure of heterogeneous materials: A double kinematics enhancement for Embedded Finite Element Method. *International Journal of Solids and Structures* 2015; 52: 180–196. doi: 10.1016/j.ijsolstr.2014.10.001

38. Jin T, Mourad HM, Bronkhorst CA, et al. Three-dimensional explicit finite element formulation for shear localization with global tracking of embedded weak discontinuities. *Computer Methods in Applied Mechanics and Engineering* 2019; 353: 416–447. doi: 10.1016/j.cma.2019.05.011

39. Grätsch T, Bathe KJ. A posteriori error estimation techniques in practical finite element analysis. *Computers & Structures* 2005; 83(4-5): 235–265. doi: 10.1016/j.compstruc.2004.08.011

40. Liu W, Yang QD, Mohammadizadeh S, Su XY, Ling DS. An accurate and efficient augmented finite element method for arbitrary crack interactions. *Journal of Applied Mechanics* 2013; 80(4): 041033.

41. Oliver J, Dias I, Huespe A. Crack-path field and strain-injection techniques in computational modeling of propagating material failure. *Computer Methods in Applied Mechanics and Engineering* 2014; 274: 289–348. doi: 10.1016/j.cma.2014.01.008

42. Jung J, Do BC, Yang QD. Augmented finite-element method for arbitrary cracking and crack interaction in solids under thermo-mechanical loadings. *Philosophical Transactions of the Royal Society A: Mathematical, Physical and Engineering Sciences* 2016; 374(2071): 20150282. doi: 10.1098/rsta.2015.0282

43. Gu YC, Jung J, Yang QD, Chen WQ. An inertia-based stabilizing method for quasi-static simulation of unstable crack initiation and propagation. *Journal of Applied Mechanics* 2015; 82(10): 101010.

44. Jung J, Yang QD. A two-dimensional augmented finite element for dynamic crack initiation and propagation. *International Journal of Fracture* 2017; 203(1-2): 41–61. doi: 10.1007/s10704-016-0129-3

45. Naderi M, Apetre N, Iyyer N. Effect of interface properties on transverse tensile response of fiber-reinforced composites: Three-dimensional micromechanical modeling. *Journal of Composite Materials* 2017; 51(21): 2963–2977. doi: 10.1177/0021998316681189

46. Naderi M, Iyyer N. 3D modeling of arbitrary cracking in solids using augmented finite element method. *Composite Structures* 2017; 160: 220–231. doi: 10.1016/j.compstruct.2016.10.061

47. Liu W, Schesser D, Yang Q, Ling D. A consistency-check based algorithm for element condensation in augmented finite element methods for fracture analysis. *Engineering Fracture Mechanics* 2015; 139: 78–97. doi: 10.1016/j.engfracmech.2015.03.038

48. Hughes TJR. *The finite element method: linear static and dynamic finite element analysis*. Englewood Cliffs, NJ: Prentice-Hall . 1987.

49. Schöberl J. NETGEN An advancing front 2D/3D-mesh generator based on abstract rules. *Computing and Visualization in Science* 1997; 1(1): 41–52. doi: 10.1007/s007910050004

50. Remacle JF, Lambrechts J, Seny B, Marchandise E, Johnen A, Geuzainet C. Blossom-Quad: A non-uniform quadrilateral mesh generator using a minimum-cost perfect-matching algorithm: QUADRILATERAL MESH GENERATOR USING PERFECT MATCHING. *International Journal for Numerical Methods in Engineering* 2012; 89(9): 1102–1119. doi: 10.1002/nme.3279

51. Geuzaine C, Remacle JF. Gmsh: A 3-D finite element mesh generator with built-in pre- and post-processing facilities. *International Journal for Numerical Methods in Engineering* 2009; 79(11): 1309–1331. doi: 10.1002/nme.2579

52. Sukumar N, Tabarraei A. Conforming polygonal finite elements. *International Journal for Numerical Methods in Engineering* 2004; 61(12): 2045–2066. doi: 10.1002/nme.1141

53. Tabarraei A, Sukumar N. APPLICATION OF POLYGONAL FINITE ELEMENTS IN LINEAR ELASTICITY. *International Journal of Computational Methods* 2006; 03(04): 503–520. doi: 10.1142/S021987620600117X

54. Mousavi SE, Xiao H, Sukumar N. Generalized Gaussian quadrature rules on arbitrary polygons. *International Journal for Numerical Methods in Engineering* 2009: n/a–n/a. doi: 10.1002/nme.2759

55. Sukumar N, Chopp DL, Moës N, Belytschko T. Modeling holes and inclusions by level sets in the extended finite-element method. *Computer Methods in Applied Mechanics and Engineering* 2001; 190(46): 6183–6200. doi: 10.1016/S0045-7825(01)00215-8

56. Chessa J, Wang H, Belytschko T. On the construction of blending elements for local partition of unity enriched finite elements. *International Journal for Numerical Methods in Engineering* 2003; 57(7): 1015–1038. doi: 10.1002/nme.777

57. Dolbow J, Harari I. An efficient finite element method for embedded interface problems. *International Journal for Numerical Methods in Engineering* 2009; 78(2): 229–252. doi: 10.1002/nme.2486

58. De Arantes E Oliveira ER. Theoretical foundations of the finite element method. *International Journal of Solids and Structures* 1968; 4(10): 929–952. doi: 10.1016/0020-7683(68)90014-0

59. Gibson RF. *Principles of composite material mechanics*. Mechanical engineering : a series of textbooks and reference booksBoca Raton London New York: CRC Press. fourth edition ed. 2016.

60. Geers MGD, Kouznetsova VG, Brekelmans WAM. Computational homogenization. In: Pippan R, Gumbsch P., eds. *Multiscale Modelling of Plasticity and Fracture by Means of Dislocation Mechanics*Vienna: Springer Vienna. 2010 (pp. 327–394)

61. Béchet E, Minnebo H, Moës N, Burgardt B. Improved implementation and robustness study of the X-FEM for stress analysis around cracks. *International Journal for Numerical Methods in Engineering* 2005; 64(8): 1033–1056. doi: 10.1002/nme.1386

62. Chessa J, Smolinski P, Belytschko T. The extended finite element method (XFEM) for solidification problems. *International Journal for Numerical Methods in Engineering* 2002; 53(8): 1959–1977. doi: 10.1002/nme.386

How to cite this article: Essongue S., G. Couégnat and E. Martin (2020), Performance assessment of the augmented finite element method for the modelling of weak discontinuities, *Int. J. Numer. Meth. Engrg.*, .